

Elemental Mercury Capture from Flue Gas by Magnetic Mn–Fe Spinel: Effect of Chemical Heterogeneity

Shijian Yang,[†] Yongfu Guo,[†] Naiqiang Yan,^{*,†} Daqing Wu,[‡] Hongping He,[‡] Zan Qu,[†] and Jinping Jia[†]

[†]School of Environmental Science and Engineering, Shanghai Jiao Tong University, 800 Dong Chuan Road, Shanghai, 200240 P. R. China

[‡]Guangzhou Institute of Geochemistry, Chinese Academy of Sciences, 511 Kehua Street, Wushan, Tianhe District, Guangzhou, 510640 P. R. China

ABSTRACT: A stoichiometric nanosized Mn–Fe spinel ($\text{Fe}_{2.2}\text{Mn}_{0.8}\text{O}_4$) was synthesized using a coprecipitation method. After the thermal treatment at 400 °C under air, chemical heterogeneity deriving from the oxidation kinetic difference between Fe^{2+} and $\text{Mn}^{2+}/\text{Mn}^{3+}$ was observed in $(\text{Fe}_{2.2}\text{Mn}_{0.8})_{1-\delta}\text{O}_4$. XPS and TEM analyses both pointed a Mn enrichment (especially Mn^{4+} cation) on the particle's surface. Furthermore, the percent of cation vacancy on the surface increased obviously due to the enrichment of Mn^{4+} cation on the surface. As a result, the capacity of $(\text{Fe}_{2.2}\text{Mn}_{0.8})_{1-\delta}\text{O}_4$ -400 for elemental mercury capture was generally much better than those of $\text{MnO}_x/\gamma\text{-Fe}_2\text{O}_3$, $(\text{Fe}_{2.2}\text{Mn}_{0.8})_{1-\delta}\text{O}_4$ -200 and $\text{Fe}_{2.2}\text{Mn}_{0.8}\text{O}_4$. Furthermore, the saturation magnetization of $(\text{Fe}_{2.2}\text{Mn}_{0.8})_{1-\delta}\text{O}_4$ obviously increased after the thermal treatment under air at 400 °C, which made it easier to separate the sorbent and adsorbed mercury from the fly ash for recycling, regeneration, and safe disposal of the adsorbed mercury. Therefore, $(\text{Fe}_{2.2}\text{Mn}_{0.8})_{1-\delta}\text{O}_4$ -400 may be a promising sorbent for elemental mercury capture.

1. INTRODUCTION

The emission of mercury from anthropogenic activities is a serious concern in both developed and developing countries.¹ Coal-fired utilities are the main source of mercury emission from anthropogenic activities. Gaseous elemental mercury is the major mercury species in the exhaust gas of coal-fired utilities.² The control of elemental mercury emission studied to date mainly falls into one of two groups: powder activated carbon (PAC) injection³ and cobenefit of selective catalytic reduction (SCR) of NO_x .⁴ The involved oxidants are mainly chlorine, and the heterogeneous oxidation involves the surface-mediated conversion of Hg^0 to HgCl_2 .⁵ For PAC injection, the formed $\text{HgCl}_2/\text{HgBr}_2$ is mainly bound to the surface of PAC, and then it can be efficiently captured by downstream particulate control devices.⁶ For SCR catalyst, the formed HgCl_2 released as gaseous HgCl_2 , and then it can be efficiently captured by wet flue gas desulfurization (FGD) systems.⁷

SCR catalysts are currently restricted in elemental mercury oxidation for at least three reasons: the concentration of HCl in the flue gas, the interference of NH_3 , and removal of toxin from industrial waste. First, the concentration of HCl may be very low in the flue gas. HCl in the flue gas results from the feed coal. In China, the chlorine content in feed-coal varies from 63 to 318 mg kg^{-1} , which is much lower than the average value of US coals (628 mg kg^{-1}).⁸ So the injection of HCl into the flue gas is sometimes necessary to improve the oxidization efficiency of elemental mercury. Second, the injection of ammonia for the necessary NO_x control is a severe interferent for elemental mercury oxidization.⁹ Third, the oxidized mercury formed (i.e., HgCl_2) is mainly present in the FGD materials. Recently, laboratory investigation found that Hg can release from FGD materials to the air over time with the addition of water.¹⁰

Now, PAC is also restricted in the application. The spent sorbent for this particular application is generally collected as a

mixture with greater than 99% of ultrafine fly ash particles by particulate control devices such as fabric filters or electrostatic precipitators (ESPs).¹¹ It will be extremely difficult and impractical to reclaim the spent sorbent from the fly ash mixture for recycling. If the contaminated fly ash is used as a cement additive, mercury may be released in the cement plant during the calcination process. Furthermore, the cost of elemental mercury control via PAC is estimated to range from 0.14 to 3.92 mills kWh^{-1} ,¹² which limits the widespread use of this technique, especially in developing countries.

In addition to chlorine, the residual O_2 in the flue gas can oxidize elemental mercury.^{13,14} Meanwhile, the oxidized mercury formed (HgO or Hg_2O) is in a solid state at <300 °C, so it adsorbs on the catalyst/sorbent and is then removed from the flue gas.³ Therefore, oxidation of elemental mercury using residual O_2 in the flue gas as the oxidant is an economical and environment-friendly method for the control of elemental mercury emission. Furthermore, the separation of sorbent and adsorbed mercury from the fly ash can be achieved by the magnetic property of sorbent.^{11,15}

Over the past few years, stoichiometric Mn–Fe spinel nanoparticles ($\text{Fe}_{3-x}\text{Mn}_x\text{O}_4$) have attracted considerable attention due to their excellent performance as catalysts.¹⁶ Nonstoichiometric Mn–Fe spinel $(\text{Fe}_{3-x}\text{Mn}_x)_{1-\delta}\text{O}_4$ can be obtained by the oxidation of $\text{Fe}_{3-x}\text{Mn}_x\text{O}_4$. An equivalent number of cation vacancies (\square) are incorporated to maintain the spinel structure during the oxidation.¹⁷ Cation vacancies on the surface are typical Lewis acid sites. Gaseous elemental mercury is a Lewis base because it can be an electron-pair donor. The term Lewis

Received: May 7, 2011

Accepted: July 6, 2011

Revised: June 27, 2011

Published: July 06, 2011

base is more general and refers to the propensity to complex with a Lewis acid, so cation vacancies on the surface can provide the active sites for the physical adsorption of elemental mercury. Meanwhile, Mn^{4+} cations on the surface are excellent oxidizing agents for the oxidization of physically adsorbed elemental mercury. Furthermore, its magnetic property makes it possible to be separated from the fly ash for recycle and safe disposal of the adsorbed mercury. In our previous research, magnetic Mn–Fe spinel was developed to capture elemental mercury from the flue gas.¹⁸ $(\text{Fe}_{2.2}\text{Mn}_{0.8})_{1-\delta}\text{O}_4$ showed an excellent capacity for elemental mercury capture, and the presence of a high concentration of SO_2 only showed a modest effect on elemental mercury capture. Our previous research also demonstrated that the capacity of $(\text{Fe}_{3-x}\text{Mn}_x)_{1-\delta}\text{O}_4$ for elemental mercury capture was approximately proportional to the product of BET, the concentrations of Mn^{4+} , and cation vacancies (\square) on the surface.¹⁸

However, the incorporation of other cations into spinel ferrite may obviously reduce its magnetization,¹⁹ which may make it difficult to separate the sorbent from the fly ash using magnetic separation. Although the magnetization can increase after the thermal treatment due to the recrystallization, the BET surface area will obviously decrease. As a result, its capacity for elemental mercury capture may obviously decrease.

Recently, chemical heterogeneity in nanosized $(\text{Fe}_{3-x}\text{Ti}_x)_{1-\delta}\text{O}_4$ resulting from the thermal treatment of $\text{Fe}_{3-x}\text{Ti}_x\text{O}_4$ under air was observed.²⁰ During the oxidation of Fe^{2+} in nanosized $\text{Fe}_{3-x}\text{Ti}_x\text{O}_4$ to form $(\text{Fe}_{3-x}\text{Ti}_x)_{1-\delta}\text{O}_4$, Fe–Ti segregation happens and Fe^{3+} cations enrich on the surface.²⁰ If Fe–Mn segregation happens in $(\text{Fe}_{3-x}\text{Mn}_x)_{1-\delta}\text{O}_4$ during the thermal treatment under air, the enrichment of Mn^{4+} cations and cation vacancies on the surface may compensate for the negative influence of the decrease of BET surface area on elemental mercury capture.

Herein, the chemical heterogeneity (i.e., the enrichment of Mn^{4+} cations and cation vacancies on the surface) in $(\text{Fe}_{3-x}\text{Mn}_x)_{1-\delta}\text{O}_4$ after the thermal treatment under air at 400 °C was demonstrated. Then, the effect of chemical heterogeneity on elemental mercury capture by $(\text{Fe}_{3-x}\text{Mn}_x)_{1-\delta}\text{O}_4$ was investigated.

2. EXPERIMENTAL SECTION

2.1. Sorbent Preparation. Nanosized $\text{Fe}_{2.2}\text{Mn}_{0.8}\text{O}_4$ was prepared using a coprecipitation method.^{18,21} Suitable amounts of ferrous sulfate, ferric trichloride, and manganous sulfate were dissolved in distilled water (the total cation concentration ≈ 0.3 mol L^{-1}). This mixture was added into a sodium hydroxide solution (1.2 mol L^{-1}), leading to an instantaneous precipitation of manganese ferrites. During the reaction, the system was continuously stirred at 800 rpm. According to Mn and Fe solubility constants, the precipitate composition was the same as that in the liquid phase, which was demonstrated by the result of ICP analysis. The particles were then separated by centrifugation at 4500 rpm for 5 min and washed with distilled water followed by a new centrifugation. After 3 washings, the particles were collected and dried in a vacuum oven at 105 °C for 12 h.

$(\text{Fe}_{2.2}\text{Mn}_{0.8})_{1-\delta}\text{O}_4$ -200 and -400 were obtained after the thermal treatment of $\text{Fe}_{2.2}\text{Mn}_{0.8}\text{O}_4$ at 200 and 400 °C under air for 3 h, respectively. With the oxidation of Fe^{2+} , Mn^{2+} , and Mn^{3+} in $\text{Fe}_{2.2}\text{Mn}_{0.8}\text{O}_4$ to form $(\text{Fe}_{2.2}\text{Mn}_{0.8})_{1-\delta}\text{O}_4$, some cation vacancies were introduced to maintain the spinel structure.¹⁷

Furthermore, $\text{MnO}_x/\gamma\text{-Fe}_2\text{O}_3$ was synthesized as a comparison, in which the ratio of Mn to Fe was about 1:2.²²

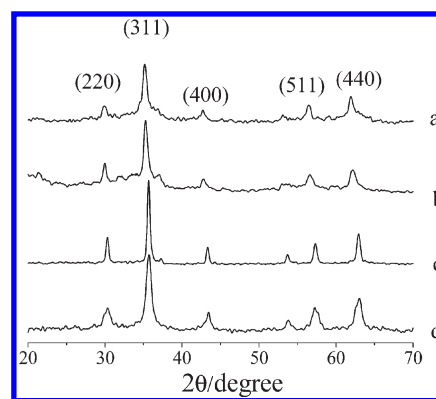


Figure 1. XRD patterns of synthesized: (a), $\text{Fe}_{2.2}\text{Mn}_{0.8}\text{O}_4$; (b), $(\text{Fe}_{2.2}\text{Mn}_{0.8})_{1-\delta}\text{O}_4$ -200; (c), $(\text{Fe}_{2.2}\text{Mn}_{0.8})_{1-\delta}\text{O}_4$ -400; (d), $\text{MnO}_x/\gamma\text{-Fe}_2\text{O}_3$.

2.2. Sorbent Characterization. X-ray diffraction (XRD) pattern was recorded on an X-ray diffractionmeter (BRUKER-AXS) between 20° and 70° at a step of 2° min^{-1} operating at 35 KV and 30 mA using Cu $K\alpha$ radiation. BET surface area was determined using a nitrogen adsorption apparatus (Micromeritics, ASAP 2010 M+C). All the samples were outgassed at 200 °C before BET measurements. Saturation magnetization was determined using a vibrating sample magnetometer (VSM, Model JDM-13) at room temperature. Transmission electron microscopy (TEM) image was performed on a JEOL JEM-2010 TEM. The micrographs were obtained in the bright-field imaging mode at an acceleration voltage of 200 kV. X-ray photoelectron spectroscopy (XPS, Thermo ESCALAB 250) was used to determine the binding energies of Fe 2p, Mn 2p, O 1s, and Hg 4f with Al $K\alpha$ ($h\nu = 1486.6$ eV) as the excitation source. The C 1s line at 284.6 eV was taken as a reference for the binding energy calibration.

2.3. Elemental Mercury Capture. The assembly used for elemental mercury capture was similar to that in our previous research.^{18,22} The gas containing elemental mercury passed through the blank tube and then entered the cold vapor atomic absorption spectrometer (CVAAS) to determine the baseline. When the concentration of elemental mercury had fluctuated within $\pm 5\%$ for more than 30 min, the gas was shifted to the tube containing some sorbent for the test. An exact amount of sorbent was inserted in the middle of the column reactor and then packed with quartz wool to support the sorbent layer and avoid its loss. It was demonstrated that quartz wool has no ability for elemental mercury capture.²³

The gas composition was as follows: 1.05 mg Nm^{-3} ($\pm 20\%$) of elemental mercury, 2% of H_2O , and balance of air. The gas flow was 12 L h^{-1} . The time for each test was about 10 h. The sorbent mass was 25.0 mg (the gas space velocity was about 6×10^5 h^{-1}), and the reaction temperatures varied from 100 to 300 °C.

The concentration of gaseous elemental mercury was analyzed online using a SG-921 CVAAS. Meanwhile, the concentration of oxidized mercury in the gas at the exit of reactor was determined using the Ontario Hydro Method.⁸

3. RESULTS AND DISCUSSION

3.1. Characterization. **3.1.1. XRD.** XRD patterns of synthesized samples are shown in Figure 1. Their characteristic peaks

Table 1. Crystal Size, Lattice Parameter, and BET Surface Area of Synthesized Samples

sample	crystal size (nm)	lattice parameter (nm)	BET surface area (m ² g ⁻¹)
Fe _{2.2} Mn _{0.8} O ₄	12	0.8456	159
(Fe _{2.2} Mn _{0.8}) _{1-δ} O ₄ -200	18	0.8431	107
(Fe _{2.2} Mn _{0.8}) _{1-δ} O ₄ -400	31	0.8346	37.8
MnO _x /γ-Fe ₂ O ₃	8.3	0.8345	77.8

corresponded very well to the standard card of maghemite (JCPDS: 39-1346). Additional peaks that would indicate the presence of other crystalline manganese oxides, such as Mn₃O₄ (hausmannite), Mn₂O₃ (bixbyite) or MnO₂, were not present in the diffraction scan. The lattice parameter of synthesized Fe_{2.2}Mn_{0.8}O₄ (shown in Table 1) was much bigger than that of magnetite (0.8396 nm) because the radiuses of Mn²⁺ (0.80 Å) and Mn³⁺ (0.66 Å) are bigger than those of Fe²⁺ (0.74 Å) and Fe³⁺ (0.64 Å), respectively. They both indicate that Mn cations were incorporated into the spinel structure of Fe_{2.2}Mn_{0.8}O₄. Due to the oxidation of Fe²⁺, Mn²⁺, and Mn³⁺, the lattice parameter of synthesized Fe_{2.2}Mn_{0.8}O₄ decreased after the thermal treatment at 200 and 400 °C under air (shown in Table 1). Crystal sizes of synthesized samples were calculated with the Scherrer's equation. The crystal size of Fe_{2.2}Mn_{0.8}O₄ increased obviously, and its BET surface area decreased obviously after the thermal treatment (shown in Table 1).

The absence of crystalline manganese oxides in MnO_x/γ-Fe₂O₃ may indicate that MnO_x was well dispersed in the composite as an amorphous phase. The lattice parameter of MnO_x/γ-Fe₂O₃ was equal to that of pure maghemite. It may indicate that few Mn cations were incorporated into the structure of γ-Fe₂O₃.²²

3.1.2. XPS. Surface information of synthesized samples was analyzed using XPS. XPS spectra over the spectral regions of Fe 2p, Mn 2p, and O 1s are shown in Figure 2.

The O 1s peak mainly centered at about 529.8 eV, as expected for the transition metal oxides. Other oxygen species at about 531.2 eV was also observed in the XPS spectra, which was assigned to -OH. Furthermore, a prominent peak (about 532.2 eV) only appeared in the XPS spectra of Fe_{2.2}Mn_{0.8}O₄ and (Fe_{2.2}Mn_{0.8})_{1-δ}O₄-200, which was ascribed to adsorbed H₂O. The percent of adsorbed H₂O decreased obviously after the thermal treatment at 200 °C for 3 h. Finally, it disappeared after the thermal treatment at 400 °C for 3 h.

The Fe species were assigned to oxidized Fe species, more likely Fe³⁺ type species. The binding energies centered at about 710.0 and 711.3 eV may be attributed to Fe³⁺ cations in the spinel structure, and the binding energy centered at 712.3 eV may be assigned to Fe³⁺ cations bonded with hydroxyl groups.

The Mn species on Fe_{2.2}Mn_{0.8}O₄ were assigned to Mn²⁺ (640.4 eV) and Mn³⁺ (641.6 eV), and Mn⁴⁺ did not appear. After the thermal treatment, Mn⁴⁺ (642.4 eV) appeared and Mn²⁺ disappeared. On MnO_x/γ-Fe₂O₃, most of the Mn cations presented as Mn⁴⁺ cations (642.3 eV) and a small amount of Mn³⁺ cations (641.3 eV) still presented.

Chemical heterogeneity can be studied by comparing the average chemical composition and the surface Fe/Mn-ratio. The average chemical composition was obtained from ICP analysis. The surface ratio of Fe to Mn resulted from XPS analysis.²⁰ The percents of Fe and Mn species on the surface

from XPS analysis are shown in Table 2. The surface Fe/Mn ratios of Fe_{2.2}Mn_{0.8}O₄ (3.0) and (Fe_{2.2}Mn_{0.8})_{1-δ}O₄-200 (2.9) were close to the average chemical composition (2.75). However, the surface Fe/Mn ratio of (Fe_{2.2}Mn_{0.8})_{1-δ}O₄-400 decreased to about 1.1. As shown in Table 2, a Mn enrichment (especially Mn⁴⁺ cation enrichment) on the surface happened after the thermal treatment at 400 °C under air. The similar phenomenon was once observed in nanosized titanomaghemite.²⁰ But in that case, an Fe enrichment on the surface was observed. The chemical heterogeneity in (Fe_{2.2}Mn_{0.8})_{1-δ}O₄-400 may be attributed to the Mn-Fe segregation, which resulted from the oxidation kinetic difference between Fe²⁺ cations and Mn²⁺/Mn³⁺ cations.

The electrical property of stoichiometric Mn-Fe spinel is similar to that of magnetite, and its band gap is very small (0.04 to 0.1 eV). Hence, it has the lower resistivity and its conductivity is almost metallic.^{19,24} Fe²⁺, Fe³⁺, Mn²⁺, and Mn³⁺ in edge sharing octahedra/tetrahedra are close together, as a result the holes and cations can migrate easily.²⁴ This may account for the good conductivity. Therefore, the oxidation of Mn-Fe spinel proceeded by the outward migration of Fe²⁺, Mn²⁺, and Mn³⁺ cations toward the surface to be oxidized, together with the incorporation of cation vacancies and the addition of oxygen atoms.²⁴ At 200 °C, Fe²⁺, Mn²⁺, and Mn³⁺ cations all diffused toward the surface of the new unit cells (shown in Figure 3a). Therefore, the chemical heterogeneity was not observed in (Fe_{2.2}Mn_{0.8})_{1-δ}O₄-200 (shown in Figure 3b). Because most of the Fe²⁺ cations were soon oxidized, the cations diffusing toward the surface were mainly Mn³⁺ and Mn²⁺ cations at 400 °C (shown in Figure 3c). Therefore, Mn cations especially Mn⁴⁺ cations enriched on the surface and Fe³⁺ cations predominated in the core of the particles (shown in Figure 3d).

3.1.3. TEM. Synthesized Fe_{2.2}Mn_{0.8}O₄ consisted of many extremely small particles (<10 nm) agglomerated to form some irregularly shaped particles (shown in Figure 4a). Selected area electron diffraction patterns (SAED) show obvious diffuse diffraction rings, as a consequence of the small crystallite sizes, that can be ascribed to the reflections of the (200), (311), (400), (511), and (440) crystallographic planes of a cubic Mn-Fe spinel phase. It demonstrates that the extremely small particles were not amorphous iron-Mn hydroxide. After the thermal treatment at 200 °C, the amount of extremely small particles decreased due to the recrystallization. Meanwhile, some bigger crystals with the particle size of 20–30 nm can be observed (shown in Figure 4b). The appearance of extremely small particles in Fe_{2.2}Mn_{0.8}O₄ and (Fe_{2.2}Mn_{0.8})_{1-δ}O₄-200 may be related to the presence of adsorbed H₂O, which may restrain the recrystallization. TEM image of (Fe_{2.2}Mn_{0.8})_{1-δ}O₄-400 (Figure 4c) reveals irregular agglomerated near spherical nanoparticles with the particle size of 20–40 nm.

Chemical heterogeneity in (Fe_{2.2}Mn_{0.8})_{1-δ}O₄-400 can also be supported by the TEM image. Figure 4c confirms that the core/shell structure appeared in many particles of (Fe_{2.2}Mn_{0.8})_{1-δ}O₄-400. As shown in the insert of Figure 4c, the core appeared with a darker contrast than the shell due to the difference in electron penetration efficiency arising from the chemical composition. The core may be ascribed to γ-Fe₂O₃, and the shell may be assigned to a large amount of Mn⁴⁺ doped γ-Fe₂O₃. Because more oxygen was incorporated into the structure of Mn⁴⁺ doped γ-Fe₂O₃, the average atomic number of the core was much more than that of the shell. As a result, the core shell contrast formed.

TEM image of MnO_x/γ-Fe₂O₃ (Figure 4d) reveals irregular agglomerated near spherical nanoparticles with the particle size

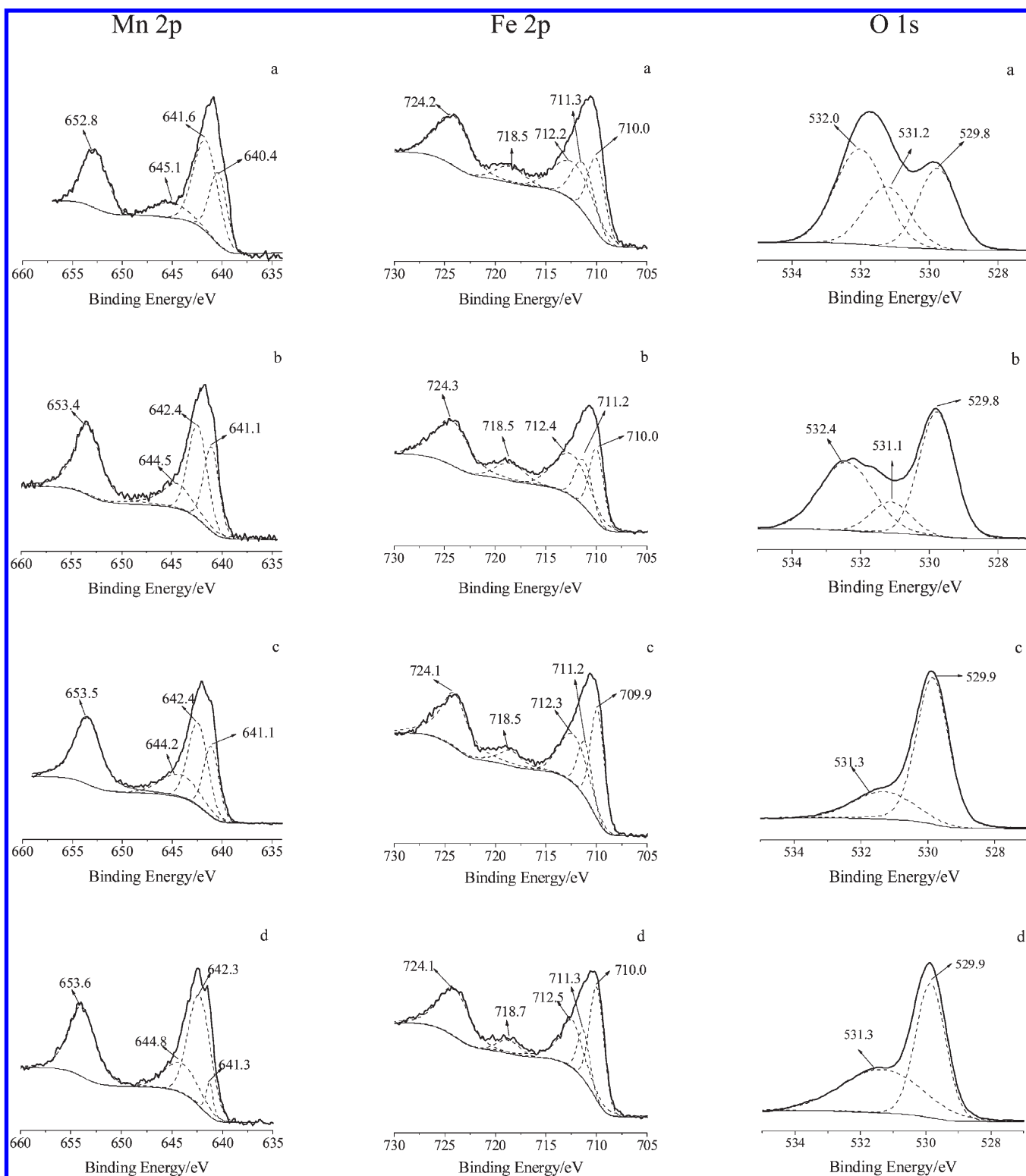


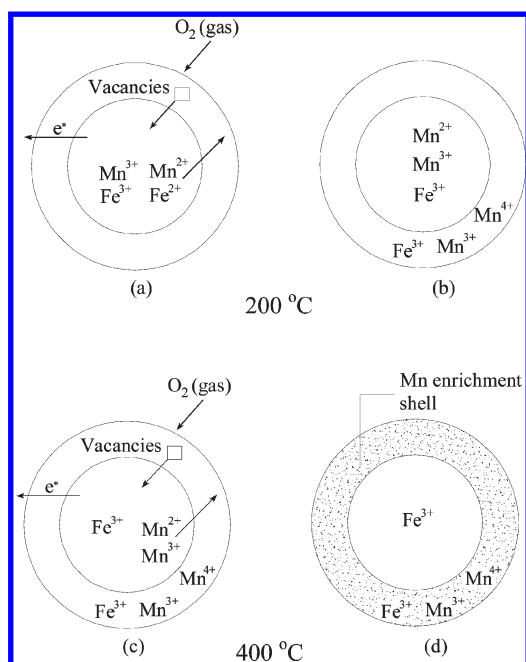
Figure 2. XPS spectra of (a), $\text{Fe}_{2.2}\text{Mn}_{0.8}\text{O}_4$; (b), $(\text{Fe}_{2.2}\text{Mn}_{0.8})_{1-\delta}\text{O}_4\text{-200}$; (c), $(\text{Fe}_{2.2}\text{Mn}_{0.8})_{1-\delta}\text{O}_4\text{-400}$; (d), $\text{MnO}_x/\gamma\text{-Fe}_2\text{O}_3$.

of 10–15 nm. It is worth mentioning that the particles were not composed of a monocrystallite, since the average crystal size obtained from XRD analysis was much smaller than the particle size in TEM image. It suggests that the particles with the size of 10–15 nm were crystalline $\gamma\text{-Fe}_2\text{O}_3$ wrapped with amorphous MnO_x .

3.2. Elemental Mercury Capture. The determination of oxidized mercury in the gas at the exit of reactor showed that there was little oxidized mercury in the gas after passing through the reactor tube with the magnetic sorbents. Therefore, the amount of elemental mercury reduced in the breakthrough curves (not shown) was captured by the magnetic sorbents.

Table 2. Data of Atomic Ratios Collected from XPS/%

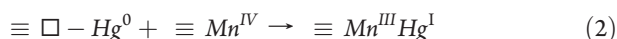
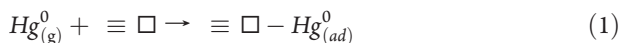
sample	[≡□]	Fe	Mn	Mn ²⁺	Mn ³⁺	Mn ⁴⁺
Fe _{2.2} Mn _{0.8} O ₄	2.0	16.4	5.3	1.9	3.4	-
(Fe _{2.2} Mn _{0.8}) _{1-δ} O ₄ -200	6.5	22.1	7.6	-	3.2	4.4
(Fe _{2.2} Mn _{0.8}) _{1-δ} O ₄ -400	8.2	20.3	18.5	-	7.2	11.3
MnO _x /γ-Fe ₂ O ₃	2.5	19.6	15.1	-	1.6	13.5


 Figure 3. Oxidation schemes of Fe_{2.2}Mn_{0.8}O₄ at 200 and 400 °C.

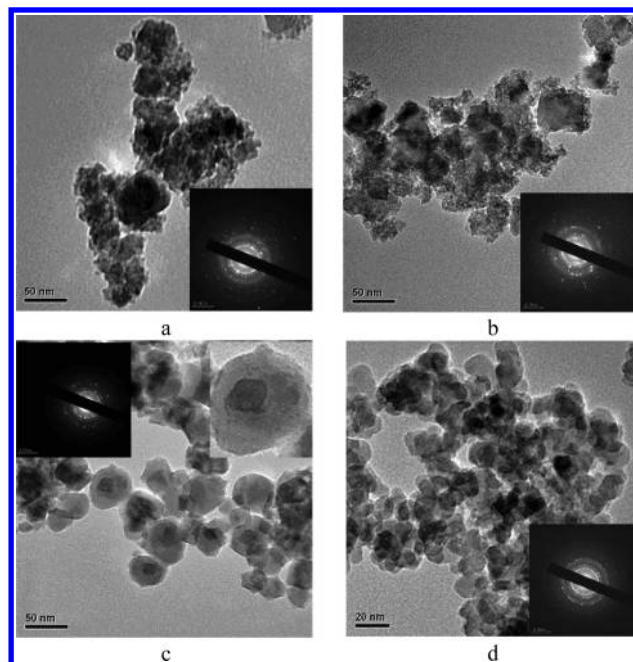
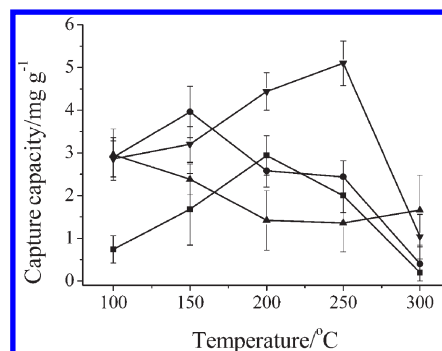
The amount of elemental mercury captured per unit mass of sorbent can be calculated from the breakthrough curve.

Figure 5 shows the capacities of Fe_{2.2}Mn_{0.8}O₄, (Fe_{2.2}Mn_{0.8})_{1-δ}O₄-200, (Fe_{2.2}Mn_{0.8})_{1-δ}O₄-400, and MnO_x/γ-Fe₂O₃ for elemental mercury capture as a function of temperature. The optimal reaction temperatures of Fe_{2.2}Mn_{0.8}O₄, MnO_x/γ-Fe₂O₃, (Fe_{2.2}Mn_{0.8})_{1-δ}O₄-200, and (Fe_{2.2}Mn_{0.8})_{1-δ}O₄-400 centered at 200, 100, 150, and 250 °C, respectively. The capacity of (Fe_{2.2}Mn_{0.8})_{1-δ}O₄-400 for elemental mercury capture was generally higher than those of MnO_x/γ-Fe₂O₃, (Fe_{2.2}Mn_{0.8})_{1-δ}O₄-200 and Fe_{2.2}Mn_{0.8}O₄.

Elemental mercury capture by metal oxides may be attributed to the Mars-Maessen mechanism.^{3,4,18} Taking into account the binding energy of Hg 4f 7/2 at 100.1 eV and the absence of Hg 4f 5/2 at about 105 eV (shown in Figure 6a), the oxidized mercury formed on (Fe_{2.2}Mn_{0.8})_{1-δ}O₄ may be mercurous oxide. Therefore, the mechanism for elemental mercury capture by (Fe_{2.2}Mn_{0.8})_{1-δ}O₄ can be described as¹⁸



Reaction 1 was the collision of elemental mercury with the surface, resulting in a physical adsorption on the cation vacancies. Reaction 2 was the oxidation of physically adsorbed elemental mercury by Mn⁴⁺ cation on the surface to form a Mn–Hg


 Figure 4. TEM images of synthesized: (a), Fe_{2.2}Mn_{0.8}O₄; (b), (Fe_{2.2}Mn_{0.8})_{1-δ}O₄-200; (c), (Fe_{2.2}Mn_{0.8})_{1-δ}O₄-400; (d), MnO_x/γ-Fe₂O₃.

 Figure 5. Capacity for elemental mercury capture: ■, Fe_{2.2}Mn_{0.8}O₄; ●, (Fe_{2.2}Mn_{0.8})_{1-δ}O₄-200; ▼, (Fe_{2.2}Mn_{0.8})_{1-δ}O₄-400; ▲, MnO_x/γ-Fe₂O₃.

bimetal oxide. Our previous research demonstrated that the capacity of (Fe_{3-x}Mn_x)_{1-δ}O₄ for elemental mercury capture was approximately proportional to the product of BET, the concentrations of Mn⁴⁺ and cation vacancies (□) on the surface. Although the BET surface of (Fe_{2.2}Mn_{0.8})_{1-δ}O₄ obviously decreased after the thermal treatment at 400 °C, the product of BET, the concentrations of Mn⁴⁺ and cation vacancies (□) on (Fe_{2.2}Mn_{0.8})_{1-δ}O₄-400 (0.35 m² g⁻¹) was much higher than that on (Fe_{2.2}Mn_{0.8})_{1-δ}O₄-200 (0.30 m² g⁻¹) due to the enrichment of Mn⁴⁺ cations and cation vacancies on (Fe_{2.2}Mn_{0.8})_{1-δ}O₄-400. As a result, the capacity of (Fe_{2.2}Mn_{0.8})_{1-δ}O₄-400 for elemental mercury capture was generally much better than that of (Fe_{2.2}Mn_{0.8})_{1-δ}O₄-200.

Taking into account the binding energies of Hg 4f 7/2 at 101.0 eV and 4f 5/2 at 105.1 eV (shown in Figure 6b), the oxidized mercury formed on MnO_x/γ-Fe₂O₃ was mercuric oxide (HgO). Therefore, Reaction 2 should be transformed as²²



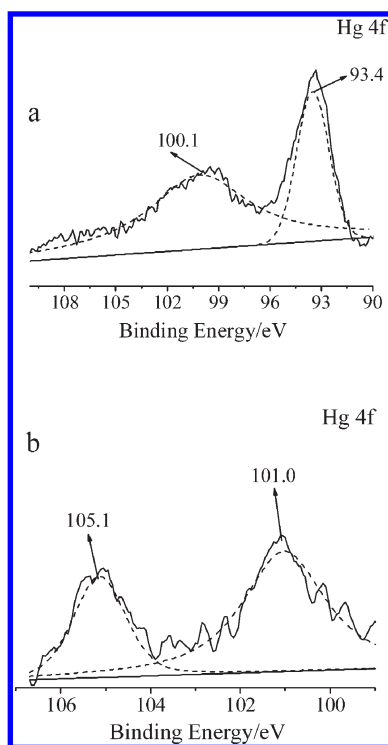


Figure 6. XPS spectra of (a), $(\text{Fe}_{2.2}\text{Mn}_{0.8})_{1-\delta}\text{O}_4$ -400 after elemental mercury capture and (b), $\text{MnO}_x/\gamma\text{-Fe}_2\text{O}_3$ after elemental mercury capture.

As shown in Reactions 2 and 3, per unit of Mn^{4+} on $(\text{Fe}_{2.2}\text{Mn}_{0.8})_{1-\delta}\text{O}_4$ can oxidize 1 unit of elemental mercury, but per unit of Mn^{4+} on $\text{MnO}_x/\gamma\text{-Fe}_2\text{O}_3$ can only oxidize 0.5 unit of elemental mercury. It indicates that the efficiency of Mn^{4+} cations on $(\text{Fe}_{2.2}\text{Mn}_{0.8})_{1-\delta}\text{O}_4$ -400 for elemental mercury oxidation was twice that on $\text{MnO}_x/\gamma\text{-Fe}_2\text{O}_3$. As a result, the capacities of $(\text{Fe}_{2.2}\text{Mn}_{0.8})_{1-\delta}\text{O}_4$ -400 and $(\text{Fe}_{2.2}\text{Mn}_{0.8})_{1-\delta}\text{O}_4$ -200 for elemental mercury capture were generally much higher than that of $\text{MnO}_x/\gamma\text{-Fe}_2\text{O}_3$ at 100–250 °C (shown in Figure 5), although $\text{MnO}_x/\gamma\text{-Fe}_2\text{O}_3$ had the highest amount of Mn^{4+} cations on its surface. Mn^{4+} cation on $(\text{Fe}_{2.2}\text{Mn}_{0.8})_{1-\delta}\text{O}_4$ may be easier to be reduced by \square to form Mn^{3+} cation at higher temperatures,¹⁷ so the capacity of $(\text{Fe}_{2.2}\text{Mn}_{0.8})_{1-\delta}\text{O}_4$ for elemental mercury capture at 300 °C was much less than that of $\text{MnO}_x/\gamma\text{-Fe}_2\text{O}_3$.

As is well-known, the radius of mercury atom (1.76 Å) is much bigger than those of Mn^{4+} , Mn^{3+} , Fe^{3+} , and O^{2-} . When a mercury atom was physically adsorbed on the cation vacancy, some ions including Mn^{4+} , Mn^{3+} , Fe^{3+} , and O^{2-} near the active site may be covered. Once the adsorbed elemental mercury contacts Mn^{4+} cation on the surface, the adsorbed elemental mercury will be oxidized. The arrays of Mn^{3+} , Fe^{3+} , Mn^{4+} , and O^{2-} in/on $(\text{Fe}_{2.2}\text{Mn}_{0.8})_{1-\delta}\text{O}_4$ were well-proportioned even at the atom scale due to the incorporation of Mn cation into the spinel structure, so the near two Mn^{4+} cations were at least spaced by two Fe^{3+} cations and four O^{2-} anions. Therefore, the distance between the near two Mn^{4+} cations on $(\text{Fe}_{2.2}\text{Mn}_{0.8})_{1-\delta}\text{O}_4$ was much more than the diameter of mercury atom. When a mercury atom was physically adsorbed on $(\text{Fe}_{2.2}\text{Mn}_{0.8})_{1-\delta}\text{O}_4$, at most one Mn^{4+} cation can be covered. As a result, Reaction 2 happened on $(\text{Fe}_{2.2}\text{Mn}_{0.8})_{1-\delta}\text{O}_4$. However, Mn^{4+} cations on $\text{MnO}_x/\gamma\text{-Fe}_2\text{O}_3$ were mainly present as amorphous MnO_2 clusters. The distance

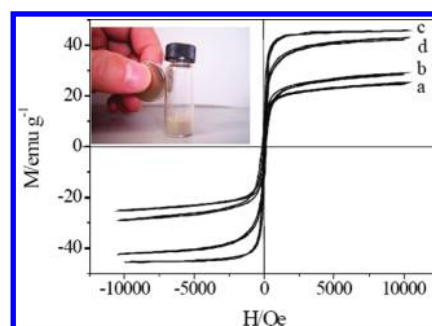


Figure 7. Magnetization characteristics of synthesized (a), $\text{Fe}_{2.2}\text{Mn}_{0.8}\text{O}_4$; (b), $(\text{Fe}_{2.2}\text{Mn}_{0.8})_{1-\delta}\text{O}_4$ -200; (c), $(\text{Fe}_{2.2}\text{Mn}_{0.8})_{1-\delta}\text{O}_4$ -400; (d), $\text{MnO}_x/\gamma\text{-Fe}_2\text{O}_3$.

between two near Mn^{4+} cations on $\text{MnO}_x/\gamma\text{-Fe}_2\text{O}_3$ was generally less than the diameter of mercury atom. When a mercury atom was physically adsorbed on $\text{MnO}_x/\gamma\text{-Fe}_2\text{O}_3$, two Mn^{4+} cations may be covered. Then, both the covered two Mn^{4+} cations oxidized the physically adsorbed mercury atom together. As a result, Reaction 3 happened on $\text{MnO}_x/\gamma\text{-Fe}_2\text{O}_3$.

3.3. Magnetic Separation of the Sorbent from the Fly Ash.

The spent sorbent for elemental mercury capture is generally collected as a mixture with greater than 99% of ultrafine fly ash particles by particulate control devices such as fabric filters or ESPs. Therefore, a key feature of $(\text{Fe}_{2.2}\text{Mn}_{0.8})_{1-\delta}\text{O}_4$ for the control of elemental mercury emission is its magnetic property, which makes it possible to separate $(\text{Fe}_{2.2}\text{Mn}_{0.8})_{1-\delta}\text{O}_4$ from the complex multiphase system for recycling, regeneration, and safe disposal of the adsorbed mercury. As shown in Figure 7, synthesized samples all showed the superparamagnetism with a minimized coercivity and a negligible magnetization hysteresis. The saturation magnetization of $\gamma\text{-Fe}_2\text{O}_3$ resulting from the thermal treatment of Fe_3O_4 under air was about 59 emu g^{-1} . The saturation magnetization of $(\text{Fe}_{2.2}\text{Mn}_{0.8})_{1-\delta}\text{O}_4$ -200 decreased to about 29 emu g^{-1} due to the incorporation of Mn. Because of the recrystallization during the thermal treatment under air at 400 °C, the saturation magnetization of $(\text{Fe}_{2.2}\text{Mn}_{0.8})_{1-\delta}\text{O}_4$ -400 increased to 46 emu g^{-1} , which made it easier to be separated from the complex multiphase system (i.e., the fly ash).

The photograph inserted in Figure 7 shows the result of separating $(\text{Fe}_{2.2}\text{Mn}_{0.8})_{1-\delta}\text{O}_4$ -400 from the mixture with 10 g of fly ash and 1 g of $(\text{Fe}_{2.2}\text{Mn}_{0.8})_{1-\delta}\text{O}_4$ -400 by a normal magnet. After $(\text{Fe}_{2.2}\text{Mn}_{0.8})_{1-\delta}\text{O}_4$ -400 was separated from the mixture, the contents of Mn and Fe in the fly ash did not increase. It indicates that $(\text{Fe}_{2.2}\text{Mn}_{0.8})_{1-\delta}\text{O}_4$ -400 can be separated from the fly ash using magnetic separation, leaving the fly ash essentially free of sorbent and adsorbed mercury.

4. CONCLUSION

Chemical heterogeneity in $(\text{Fe}_{2.2}\text{Mn}_{0.8})_{1-\delta}\text{O}_4$ -400 was demonstrated using XPS and TEM. The enrichment of Mn^{4+} cation and cation vacancy on the surface obviously promoted elemental mercury capture by $(\text{Fe}_{2.2}\text{Mn}_{0.8})_{1-\delta}\text{O}_4$. As a result, $(\text{Fe}_{2.2}\text{Mn}_{0.8})_{1-\delta}\text{O}_4$ -400 with lower BET surface area displayed an excellent ability for elemental mercury capture. Furthermore, the saturation magnetization of $(\text{Fe}_{2.2}\text{Mn}_{0.8})_{1-\delta}\text{O}_4$ after the thermal treatment under air at 400 °C obviously increased, which made it easier to separate $(\text{Fe}_{2.2}\text{Mn}_{0.8})_{1-\delta}\text{O}_4$ -400 from the fly ash for recycling, regeneration, and safe disposal of the adsorbed mercury.

In our future work, the durability (for example friability and sintering properties) of Mn–Fe spinel will be examined. Furthermore, the effect of the components in the flue gas (for example H₂O, O₂, CO₂, CO, hydrocarbons, HCl, SO₂, SO₃, NO_x, and so on) on elemental mercury capture by Mn–Fe spinel will be further investigated.

AUTHOR INFORMATION

Corresponding Author

*Phone and fax: 86-21-54745591. E-mail: nqyan@sjtu.edu.cn (N. Q. Yan), yangshijiangsq@163.com (S. J. Yang).

ACKNOWLEDGMENT

This study was supported by the High-Tech R&D Program of China (No. 2007AA06Z340), the Scholarship Award for Excellent Doctoral Student granted by Ministry of Education of China, and Shanghai Tongji Gao Tingyao Environmental Science & Technology Development Foundation.

REFERENCES

- (1) Qiao, S. H.; Chen, J.; Li, J. F.; Qu, Z.; Liu, P.; Yan, N. Q.; Jia, J. Q. Adsorption and catalytic oxidation of gaseous elemental mercury in flue gas over MnO_x/alumina. *Ind. Eng. Chem. Res.* **2009**, *48*, 3317–3322.
- (2) Lu, D. Y.; Granatstein, D. L.; Rose, D. J. Study of mercury speciation from simulated coal gasification. *Ind. Eng. Chem. Res.* **2004**, *43*, 5400–5404.
- (3) Granite, E. J.; Pennline, H. W.; Hargis, R. A. Novel sorbents for mercury removal from flue gas. *Ind. Eng. Chem. Res.* **2000**, *39*, 1020–1029.
- (4) Presto, A. A.; Granite, E. J. Survey of catalysts for oxidation of mercury in flue gas. *Environ. Sci. Technol.* **2006**, *40*, 5601–5609.
- (5) Srivastava, R. K.; Hutson, N.; Martin, B.; Princiotta, F.; Staudt, J. Control of mercury emissions from coal-fired in electric utility boilers. *Environ. Sci. Technol.* **2006**, *40*, 1385–1393.
- (6) Presto, A. A.; Granite, E. J. Impact of sulfur oxides on mercury capture by activated carbon. *Environ. Sci. Technol.* **2007**, *41*, 6579–6584.
- (7) Eswaran, S.; Stenger, H. G. Understanding mercury conversion in selective catalytic reduction (SCR) catalysts. *Energy Fuel* **2005**, *19*, 2328–2334.
- (8) Wang, S. X.; Zhang, L.; Li, G. H.; Wu, Y.; Hao, J. M.; Pirrone, N.; Sprovieri, F.; Ancora, M. P. Mercury emission and speciation of coal-fired power plants in China. *Atmos. Chem. Phys.* **2010**, *10*, 1183–1192.
- (9) Lee, C. W.; Serre, S. D.; Zhao, Y.; Lee, S. J. Mercury oxidation promoted by a selective catalytic reduction catalyst under simulated Powder River Basin coal combustion conditions. *J. Air Waste Manage.* **2008**, *58*, 484–493.
- (10) Gustin, M.; Ladwig, K. Laboratory investigation of Hg release from flue gas desulfurization products. *Environ. Sci. Technol.* **2010**, *44*, 4012–4018.
- (11) Dong, J.; Xu, Z. H.; Kuznicki, S. M. Magnetic multi-functional nano composites for environmental applications. *Adv. Funct. Mater.* **2009**, *19*, 1268–1275.
- (12) Jones, A. P.; Hoffmann, J. W.; Smith, D. N.; Feeley, T. J.; Murphy, J. T. DOE/NETL's phase II mercury control technology field testing program: Preliminary economic analysis of activated carbon injection. *Environ. Sci. Technol.* **2007**, *41*, 1365–1371.
- (13) Granite, E. J.; Pennline, H. W. Photochemical removal of mercury from flue gas. *Ind. Eng. Chem. Res.* **2002**, *41*, 5470–5476.
- (14) Granite, E. J.; Pennline, H. W.; Hoffman, J. S. Effects of photochemical formation of mercuric oxide. *Ind. Eng. Chem. Res.* **1999**, *38*, 5034–5037.
- (15) Dong, J.; Xu, Z. H.; Kuznicki, S. M. Mercury removal from flue gases by novel regenerable magnetic nanocomposite sorbents. *Environ. Sci. Technol.* **2009**, *43*, 3266–3271.
- (16) Zhang, Z. J.; Wang, Z. L.; Chakoumakos, B. C.; Yin, J. S. Temperature dependence of cation distribution and oxidation state in magnetic Mn-Fe ferrite nanocrystals. *J. Am. Chem. Soc.* **1998**, *120*, 1800–1804.
- (17) Gillot, B.; Laarj, M.; Kacim, S. Reactivity towards oxygen and cation distribution of manganese iron spinel Mn_{3-x}Fe_xO₄ (0 ≤ x ≤ 3) fine powders studied by thermogravimetry and IR spectroscopy. *J. Mater. Chem.* **1997**, *7*, 827–831.
- (18) Yang, S.; Yan, N.; Guo, Y.; Wu, D.; He, H.; Qu, Z.; Li, J.; Zhou, Q.; Jia, J. Gaseous elemental mercury capture from flue gas using magnetic nanosized (Fe_{3-x}Mn_x)_{1-δ}O₄. *Environ. Sci. Technol.* **2011**, *45*, 1540–1546.
- (19) Singh, D. J.; Gupta, M.; Gupta, R. Magnetism and electronic structure in ZnFe₂O₄ and MnFe₂O₄. *J. Appl. Phys.* **2002**, *91*, 7370–7372.
- (20) Guigue-Millot, N.; Champion, Y.; Hytch, M. J.; Bernard, F.; Begin-Colin, S.; Perriat, P. Chemical heterogeneities in nanometric titanomagnetites prepared by soft chemistry and studied ex situ: Evidence for Fe-segregation and oxidation kinetics. *J. Phys. Chem. B* **2001**, *105*, 7125–7132.
- (21) Kodama, T.; Ookubo, M.; Miura, S.; Kitayama, Y. Synthesis and characterization of ultrafine Mn(II)-bearing ferrite of type Mn_xFe_{3-x}O₄ by coprecipitation. *Mater. Res. Bull.* **1996**, *31*, 1501–1512.
- (22) Yang, S.; Guo, Y.; Yan, N.; Qu, Z.; Xie, J.; Yang, C.; Jia, J. Capture of gaseous elemental mercury from flue gas using a magnetic and sulfur poisoning resistant sorbent Mn/γ-Fe₂O₃ at lower temperatures. *J. Hazard. Mater.* **2011**, *186*, 508–515.
- (23) Li, J. F.; Yan, N. Q.; Qu, Z.; Qiao, S. H.; Yang, S. J.; Guo, Y. F.; Liu, P.; Jia, J. P. Catalytic oxidation of elemental mercury over the modified catalyst Mn/α-Al₂O₃ at lower temperatures. *Environ. Sci. Technol.* **2010**, *44*, 426–431.
- (24) Cornell, R. M.; Schwertmann, U. *The iron oxides: Structure, properties, reactions, occurrences and uses*; Wiley-VCH: New York, 2003.